
Noncontact Cable Tension Force Estimation Using an Integrated Vision and Inertial Measurement System

Abstract: In this study, a noncontact cable tension force estimation technique was developed using an integrated vision and inertial measurement system (VIS) installed at a reference point, and the movement of the VIS was explicitly considered. Cable displacement was first estimated by applying a proposed contour-based algorithm to the vision measurements. Thereafter, the movement of the VIS at the reference point was estimated from the inertial measurement system and was used to compensate the error in the previously estimated cable displacement. Finally, the cable tension force was estimated using the compensated cable displacement. The feasibility of the proposed technique was validated through a laboratory test on a full-scale pedestrian bridge cable and a field test on a single-pylon cable-stayed pedestrian bridge. Overall, the proposed technique estimated the cable tension forces reliably with less than 1.3% discrepancy compared to those estimated by accelerometers.

Keywords: Noncontact cable force estimation, computer vision, inertial measurement unit sensor, data fusion, camera motion compensation

1. Introduction

Continuous health monitoring is essential for large-scale bridges, such as cable-stayed bridges and suspension bridges, and various efforts have been made to this end [1,2]. Cables are major load-carriers for these cable-supported structures. Therefore, cable tension monitoring is vital to prevent any catastrophic failures of cable-supported structures [3]. Several cable force estimation techniques have been proposed using load cells [4,5], strain sensors [6,7], accelerometers [8–12], electromagnetic (EM) sensors [13,14], and eddy current sensors [15]. Note that, all these discrete sensors must be physically placed on each cable, but it may not be easy to access these cables for sensor installation.

Several attempts were performed to develop computer vision techniques for the noncontact tension force estimation of multiple cables [16–20]. A vision camera was installed at a stationary location with target cables visible within the field of view (FOV) of the camera. The cable displacement was first estimated from vision measurements, and the resonance frequencies of each cable were identified from the estimated displacement. Thereafter, the cable tension force was estimated based on its relationship with the cable resonance frequencies. Although several computer vision algorithms were developed for displacement estimation [21–25], majority of them required the attachment of artificial targets to

the cables. Template-matching algorithms were most commonly used for cable displacement estimation [17,18]. However, the bridge cable only occupies few pixels and often featureless, resulting in poor robustness and incorrect matching [19]. To overcome this limitation, a boundary-based algorithm estimated the cable displacement by assuming cable boundaries as two straight lines [19]. However, this assumption was invalid for a wire rope cable without a protective shell. By placing a vision camera far away from target cables, an edge-based algorithm [20] assumed that each cable is a straight line within the FOV. However, owing to the long distance between the camera and the target cables, it was difficult to estimate small displacements.

Another common issue with vision-based cable force estimation techniques is that the assumed stationary location, where the vision camera is installed, is often not fixed and indeed vibrates. This camera motion results in aggravated errors in the cable tension force estimation. A few attempts were made to compensate such camera-motion-induced errors. A common approach for camera motion compensation is to capture an additional stationary natural target within the FOV of the camera. Then, the camera motion can be compensated by subtracting the estimated camera motion from the initially captured cable displacement [17]. However, this approach has limitations, as illustrated in Figure 1 [26]. From Figure 1, we can see that when the camera moves with both translation (Δz) and rotation ($\Delta\varphi$), the corresponding camera-motion-induced error becomes $(\Delta z + \Delta\varphi l_1)$ at the target cable. However, the estimated camera-motion-induced error using a stationary natural target becomes $(\Delta z + \Delta\varphi(l_2 + l_1))$. Therefore, unless (1) the camera has only translation ($\Delta\varphi = 0$) or (2) the distance between the camera and the target cable is identical to the distance between the camera and the stationary target ($l_2 = 0$), this approach will not be fully valid. Another issue is that because the stationary target is often far away from the camera in field conditions, the camera motion estimated by the stationary target becomes inaccurate and noisy. Another approach is to compensate 6-DOF camera motions using an integrated system which includes two vision cameras [26]. Here, the integrated system must be placed very close (50 mm) to an artificial stationary target. The camera motion-induced error can be compensated by calculating the relative displacement between two measurement points within the target cable [19]. However, the relative displacement between these two points is significantly smaller than the displacement of each location, further making it difficult to identify the cable resonance frequencies.

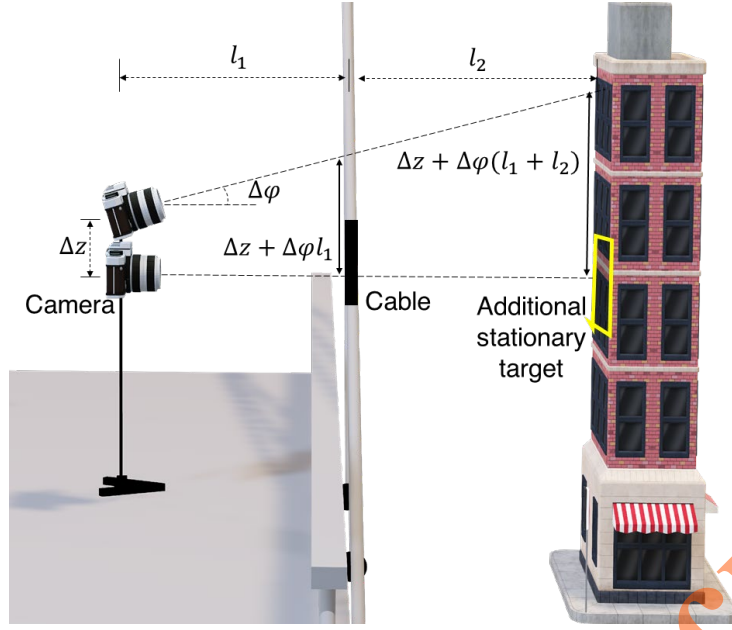


Figure 1. Limitation of camera motion compensation using an additional stationary natural target when a camera moving with both translation (Δz) and rotation ($\Delta\phi$)

This study proposes a noncontact cable tension force estimation technique using an integrated vision and inertial measurement system (VIS) installed at a vibrating reference point. A contour-based algorithm was proposed and applied to vision measurement to estimate an initial cable displacement. Then, inertial measurements were used to compensate the cable displacement error produced by the vibration of the integrated vision and inertial measurement system. Finally, the compensated cable displacement was used for estimating the cable tension force. The contribution of this study lies in the following: (1) noncontact cable tension force estimation using a VIS placed on a vibrating reference point, (2) development of a contour-based algorithm to estimate cable displacement, and (3) improvement of the accuracy of cable tension force estimation by compensating the reference point vibration.

The remainder of this paper is organized as follows: Section 2 presents the working principle of the proposed cable tension force estimation technique. The feasibility of the proposed technique was experimentally validated through a laboratory test on a full-scale pedestrian bridge cable and a field test on a single-pylon cable-stayed pedestrian bridge, which are detailed in Sections 3 and 4, respectively. The concluding remarks are provided in Section 5.

2. Development of cable tension force estimation technique

An overview of the proposed cable tension force estimation technique is depicted in Figure 2. A VIS, including a vision camera and an inertial measurement unit (IMU) sensor, was installed on a vibrating reference point near target cables with them visible within the FOV of the camera. At first, a contour-based algorithm was proposed for the initial cable displacement estimation from captured vision

images. It should be noted that this initially estimated displacement includes a camera-motion-induced error. Thereafter, the camera motion was estimated from the inertial measurement and was used to compensate the camera-motion-induced error in the previously estimated initial cable displacement. Subsequently, the cable resonance frequency was estimated from the compensated cable displacement using Fourier transform, and finally, the cable tension force was estimated from the estimated cable resonance frequency using a taut string theory. The details are provided in the following subsections.

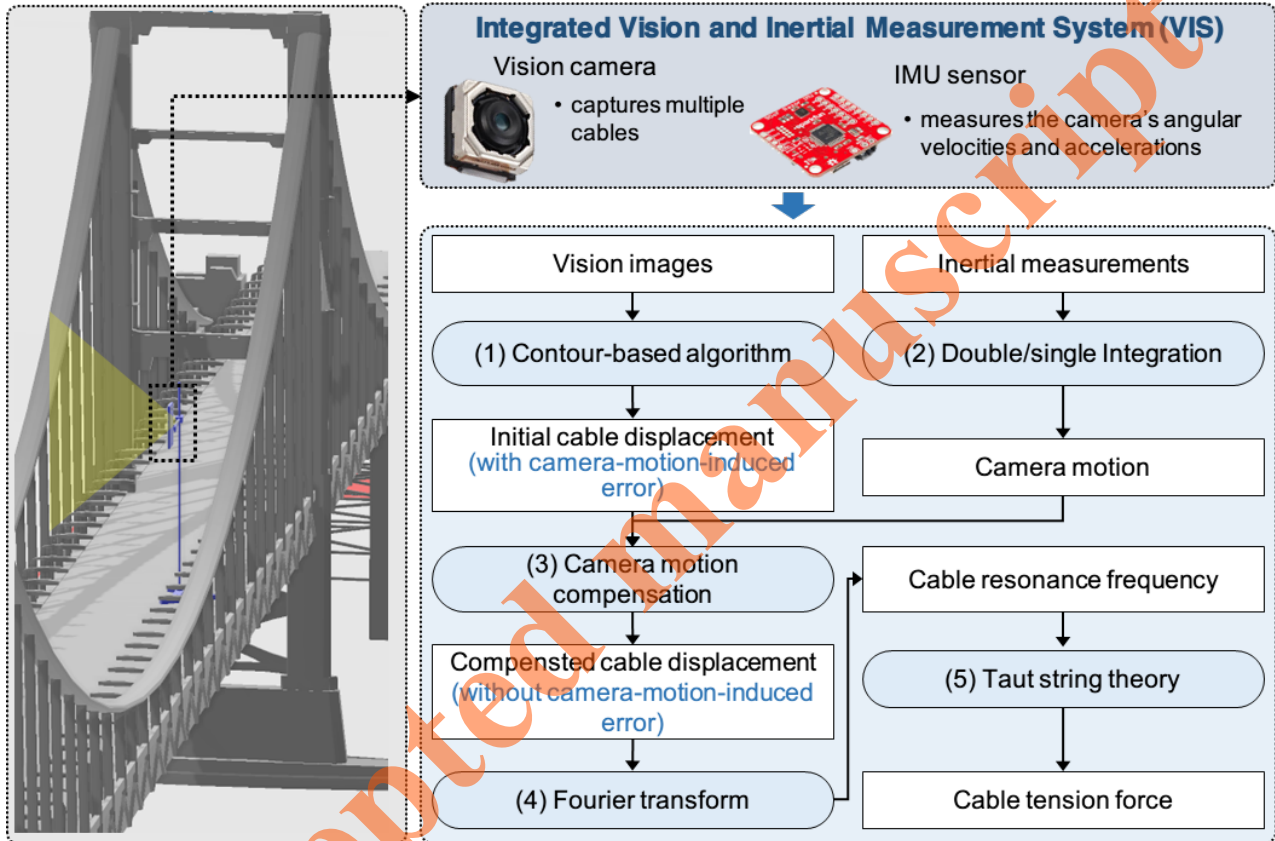


Figure 2. Overview of the proposed cable tension force estimation technique

2.1 Contour-based initial cable displacement estimation

The proposed contour-based algorithm for estimating the initial cable displacement from vision measurement is illustrated in Figure 3. The first frame image was used as a reference frame, and the proposed algorithm estimated the relative horizontal cable displacement between the first and i^{th} frames.

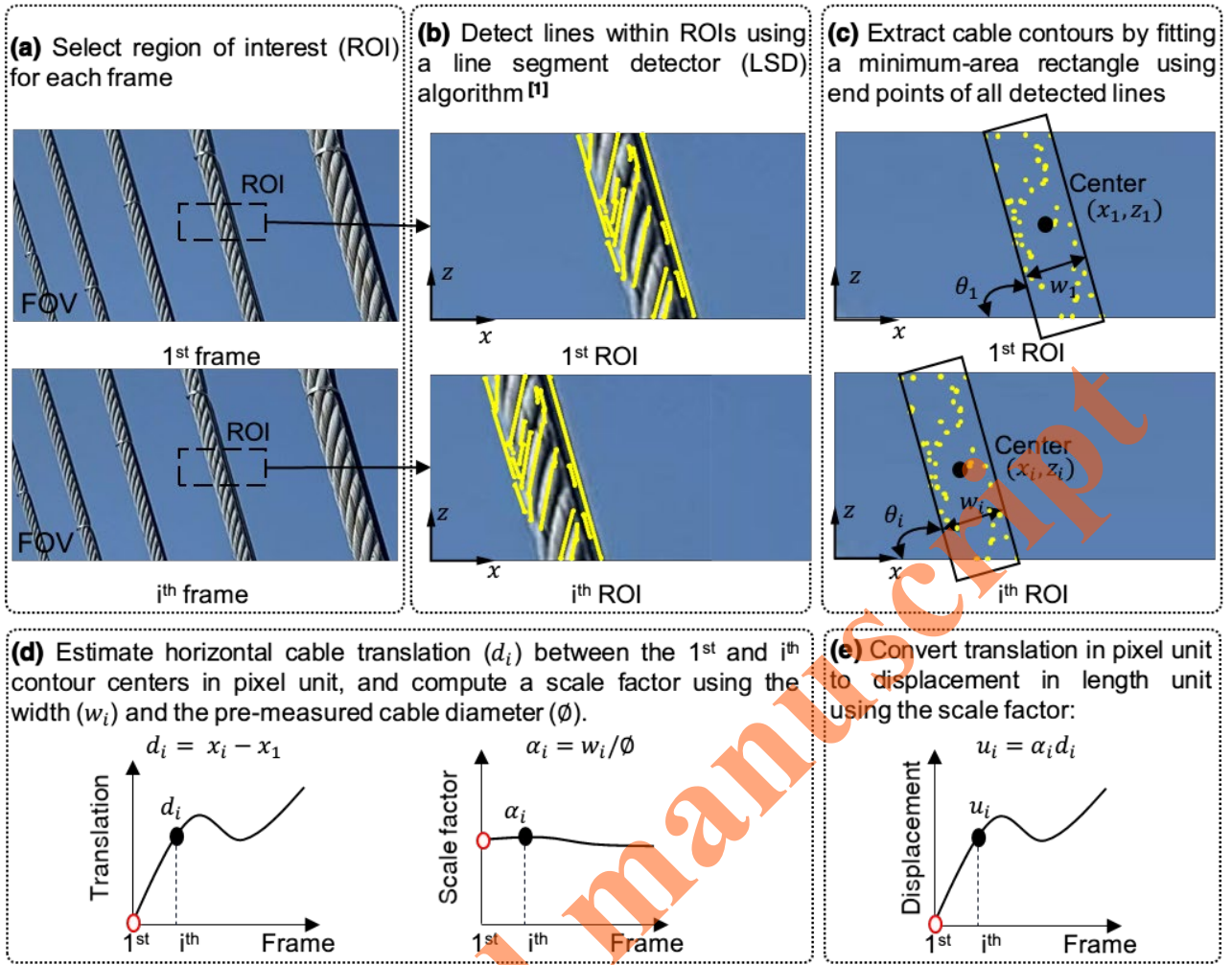


Figure 3. Proposed contour-based initial cable displacement estimation procedure

98

99

100

101

102

103

104

105

106

107

108

109

110

111

112

At first, the size and location of the ROI were manually selected for the first frame so that the target cable could be captured within the ROI, and this ROI was maintained throughout subsequent frames (Figure 3(a)). It should be noted that multiple ROIs should be selected for the simultaneous tracking of multiple cables. Thereafter, a line segment detector algorithm [27] was applied to each ROI to detect lines from the cable with subpixel accuracy. Generally, two long straight lines are not detected at both boundaries of the cable, especially for a wire rope cable without a protective shell. Instead, several short lines are detected both at the boundaries and at the surface of the cable (Figure 3(b)). Thus, a minimum-area rectangle, which embraces the end points of all detected short lines, was identified, and the rectangle was used as the cable contour (Figure 3(c)). Here, the background of the cable is assumed to be textureless, and therefore lines are detected only from the cable. In general, cables of a bridge, at least partially, have sky in their background, which makes this assumption valid. Note that the assumption was commonly used in existing studies [19,20,28]. Three features were extracted from the cable contour: the coordinates of the center point (x_i, z_i), cable width (w_i), and cable tilt angle (θ_i) (Figure 3(c)). The horizontal cable translation at the i^{th} frame, d_i , is defined as the difference of the

center point coordinates between the first and i^{th} frames in the horizontal direction (Figure 3(d)).

$$d_i = x_i - x_1 \quad (1)$$

A scale factor for converting the translation in pixels to displacement in units of length was computed using the cable width (w_i) in pixels and the pre-measured cable diameter (ϕ) in units of length (Figure 3(d)) [21].

$$\alpha_i = \frac{w_i}{\phi} \quad (2)$$

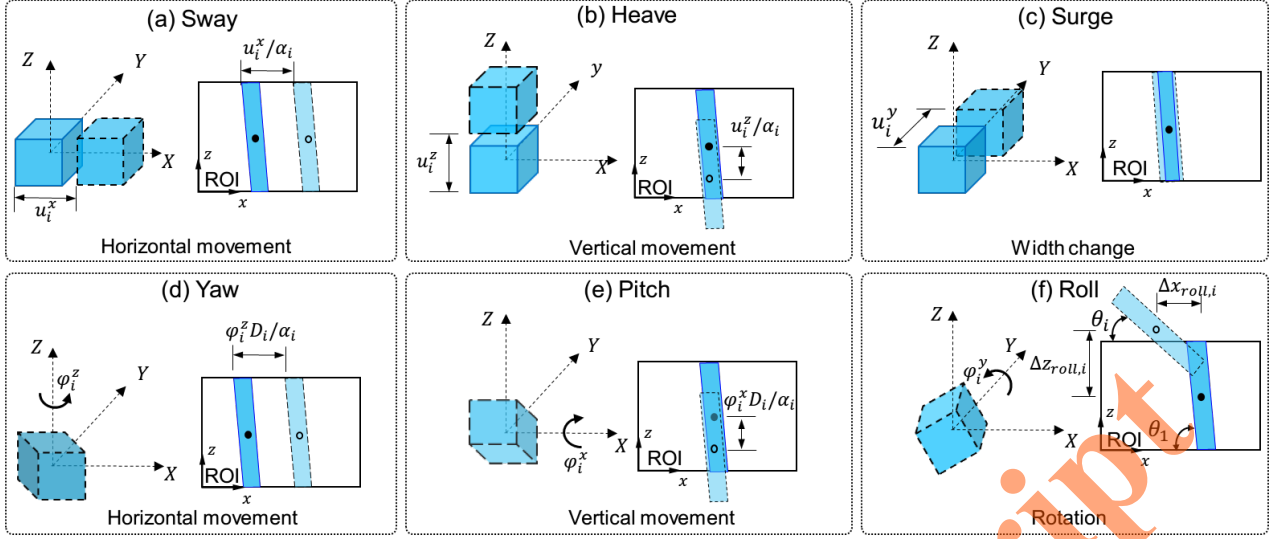
Finally, the translation was converted into displacement (u_i) using the estimated scale factor (Figure 3(e)):

$$u_i = \alpha_i d_i = \frac{w_i}{\phi} (x_i - x_1) \quad (3)$$

Considering that the true vibration direction of a cable is not purely horizontal, the proposed algorithm cannot track the same cable segment. Therefore, the estimated horizontal displacement is not equal to the horizontal component of the true cable displacement. However, the estimated horizontal displacement is proportional to the true cable displacement, and therefore does not affect the estimation of the cable modal frequency and tension force [19,20]. Figure 3 illustrates the proposed technique under a large horizontal displacement and a steep tilt angle. The technique can also be applied to a case with a large vertical displacement and a small tilt angle, and to estimate the vertical displacement of the cable instead of the horizontal displacement. It should be noted that the ROI should be selected considering: (1) the cable segment included in ROI have relatively strong vibration, and such cable segments can be selected from near the central of the cable; and (2) the background of the cable segment included in ROI is textureless.

2.2 Cable displacement and tension force estimation after camera motion compensation

Because the camera is installed on a vibrating reference point, the camera itself has its own motion. Therefore, the initial cable displacement estimated in the previous section includes this camera-motion-induced error, and this error must be compensated for reliable displacement estimation. Figure 4 depicts six different types of camera motions and their effects on the captured vision images.



D_i and α_i denote the distance between the camera and the cable and scale factor, respectively.

Figure 4. Six different types of camera motion and their effects on captured vision images: (a) sway, (b) heave, (c) surge, (d) yaw, (e) pitch, and (f) roll

The camera sway (u_i^x) and yaw (φ_i^z) produce fictitious cable movement in the horizontal direction (x-direction) ($\Delta x_{sway+yaw,i}$) (Figure 4(a) and (d)),

$$\Delta x_{sway+yaw,i} = \frac{u_i^x + \varphi_i^z D_i}{\alpha_i} \quad (4)$$

where D_i denotes the distance between the camera and the target cable. The camera heave (u_i^z) and pitch (φ_i^x) produce fictitious cable movement in the vertical direction (z-direction) ($\Delta z_{heave+pitch,i}$) (Figure 4(b) and (e)),

$$\Delta z_{heave+pitch,i} = \frac{u_i^z + \varphi_i^x D_i}{\alpha_i} \quad (5)$$

The camera surge (u_i^y) causes a change in the distance between the cable and the camera (D_i), thus resulting in a change in the cable width (w_i) (Figure 4(c)). However, u_i^z is much smaller than D_i , and then its effect on the estimated cable displacement is ignored in this study. The camera roll (φ_i^y) produces fictitious cable rotation ($\theta_1 - \theta_i$), and fictitious cable movement in both vertical and horizontal directions ($\Delta z_{roll,i}$ and $\Delta x_{roll,i}$, respectively) (Figures 4(f) and 5),

$$\begin{aligned} \Delta z_{roll,i} &= R \{ \sin(\beta_1 + \varphi_i^y) - \sin(\beta_1) \} \\ \Delta x_{roll,i} &= R \{ \cos(\beta_1 + \varphi_i^y) - \cos(\beta_1) \} \end{aligned} \quad (6)$$

$$R = \sqrt{(Z_o + z_1)^2 + (X_o + x_1)^2}; \beta_1 = \text{atan}\left(\frac{Z_o + z_1}{X_o + x_1}\right); \varphi_i^y = \theta_1 - \theta_i$$

where (x_1, z_1) denotes the coordinates of the cable center point in the 1st ROI. X_o and Z_o denote pixel distances between the center point of FOV (P) and the lower left vertex of the ROI (O) in x and z

149 directions, respectively (As shown in Figure 5). It should be noted that the fictitious vertical cable
 150 movement produces errors in the horizontal cable displacement estimation, as depicted in Figure 6.
 151 The total error in the horizontal displacement estimation produced by the camera motion is denoted as
 152 u_i^e in units of length:

$$u_i^e = \alpha_i d_i^e = \alpha_i \left(\Delta x_{\text{sway}+\text{yaw},i} + \Delta x_{\text{roll},i} + \frac{\Delta z_{\text{heave}+\text{pitch},i} + \Delta z_{\text{roll},i}}{\tan(\theta_i)} \right) \quad (7)$$

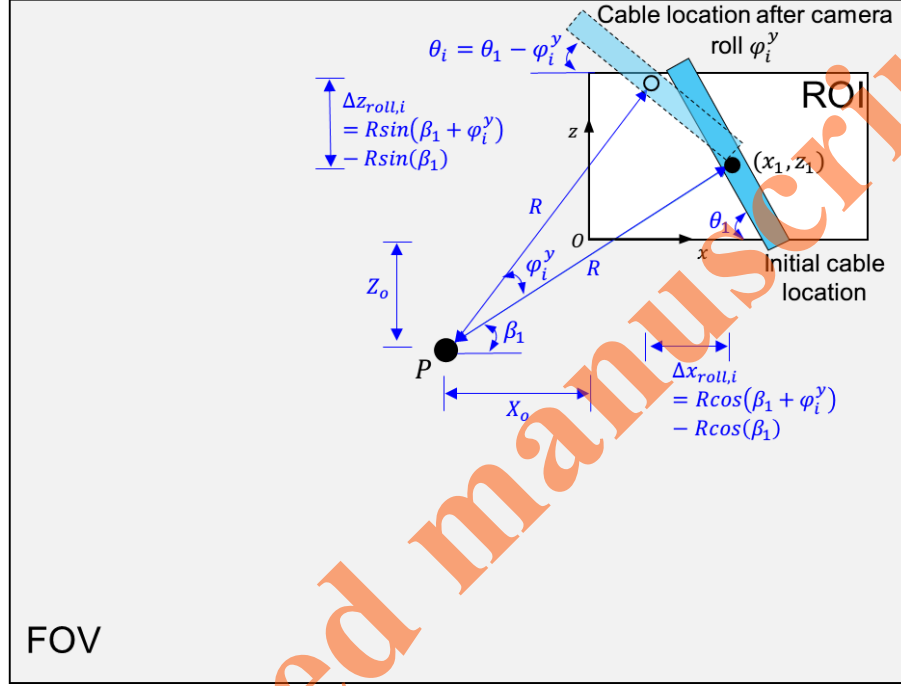


Figure 5. Fictitious cable rotation and movement induced by the camera roll

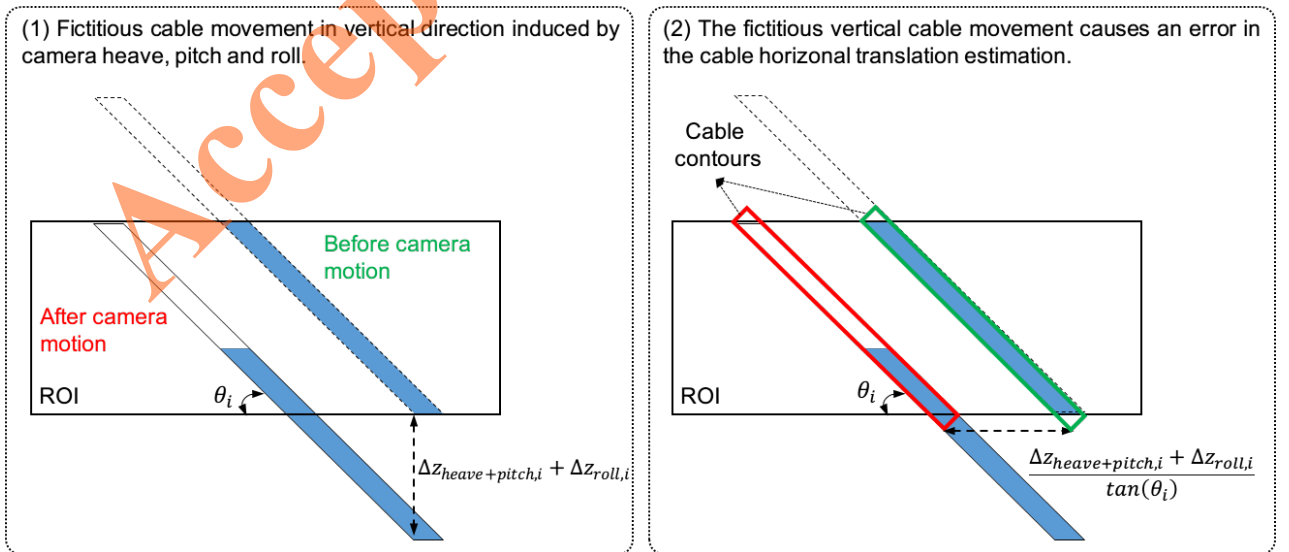


Figure 6. Error in the horizontal translation estimation induced by fictitious cable vertical movement

155

156 Then, the cable displacement after compensating camera motion becomes,

$$u_i^t = u_i - u_i^e = u_i - u_i^x - \varphi_i^z D_i - R\{\cos(\beta_1) - \cos(\beta_1 + \theta_1 - \theta_i)\} - \frac{u_i^z + \varphi_i^x D_i + R\{\sin(\beta_1) - \sin(\beta_1 + \theta_1 - \theta_i)\}}{\tan(\theta_i)} \quad (8)$$

157 The following relationship holds between the scale factor (α_i) and the distance between the camera
 158 and the target (D_i) [21]:

$$\alpha_i = \frac{D_i}{f} d_{pixel} \quad (9)$$

159 where f and d_{pixel} are the focal length and pixel size of the camera, respectively. Then, D_i can be
 160 estimated as,

$$D_i = \frac{f \alpha_i}{d_{pixel}} \quad (10)$$

161 Substituting Eq. (10) into Eq. (8) results in,

$$u_i^t = u_i - u_i^x - R\{\cos(\beta_1) - \cos(\beta_1 + \theta_1 - \theta_i)\} - \frac{u_i^z + R\{\sin(\beta_1) - \sin(\beta_1 + \theta_1 - \theta_i)\}}{\tan(\theta_i)} - \left(\varphi_i^z + \frac{\varphi_i^x}{\tan(\theta_i)} \right) \frac{w_i f}{\phi d_{pixel}} \quad (11)$$

162 u_i^x and u_i^z were estimated from the double integration of acceleration measurements, and φ_i^x and
 163 φ_i^z were estimated from the single integration of angular velocity measurements. Because the
 164 acceleration and angular velocity measurements from the IMU sensor have a higher sampling rate than
 165 vision measurements, the estimated u_i^x , u_i^z , φ_i^x and φ_i^z values were down-sampled to match the
 166 sampling rate of vision measurements. To remove low-frequency drifts in the estimated u_i^t , a high-
 167 pass filter with a cut-off frequency of 0.5 Hz was applied to u_i^t and only high-frequency components
 168 of the cable displacement was retained. Note that a smaller cut-off frequency value could be used for
 169 a high-performance IMU sensors.

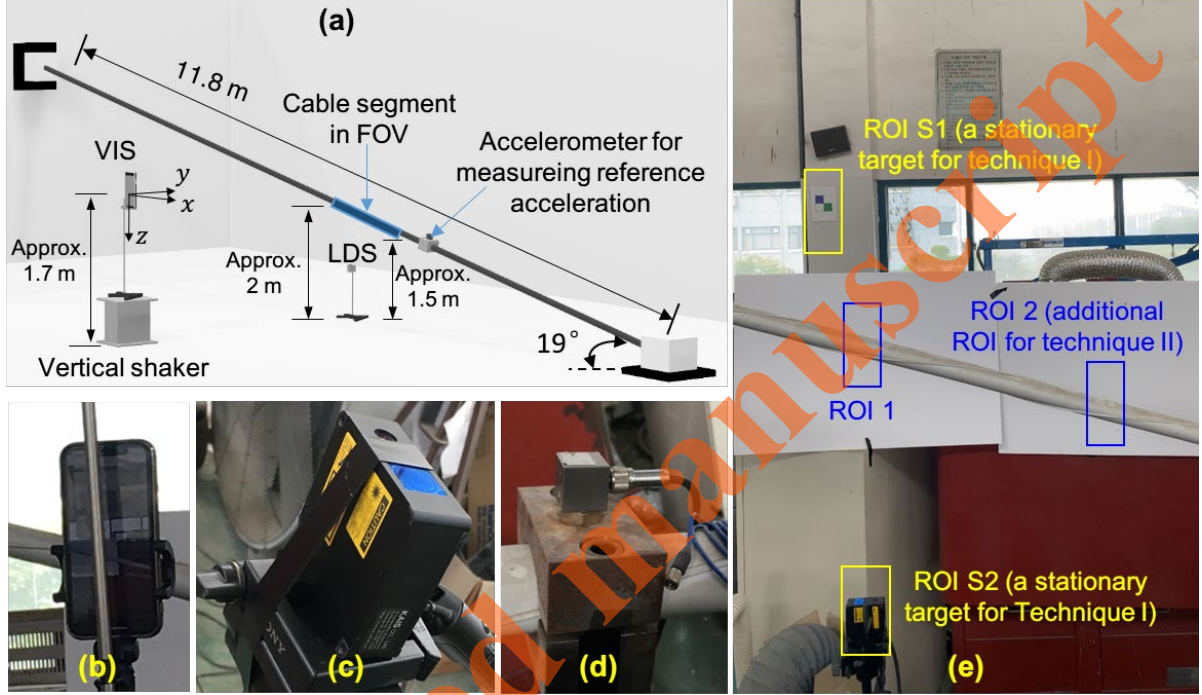
170 Finally, the resonance frequencies of the cable, which are higher than 0.5 Hz in most cases, were
 171 estimated from the frequency spectrum of the compensated cable displacement, and the tension force
 172 (T) of the cable was estimated from the measured resonance frequency based on the commonly used
 173 taut string theory [19],

$$T = 4mL^2 \left(\frac{f_n}{n} \right)^2 \quad (12)$$

where f_n represents the natural frequency, and the measured resonance frequency was used to approximate f_n . m and L denote the mass density and length of the cable, respectively.

3. Laboratory testing of a full-scale pedestrian bridge cable

3.1 Experimental setup



ROI S1 and ROI S2 are 3.8 m and 1.5 m apart from the vision-inertial system, respectively.

Figure 7. Configuration of full-scale pedestrian bridge cable test: (a) cable setup, (b) VIS, *i.e.*, iPhone 11, installed on a shaker, which is 1.5 m apart from the cable, (c) laser displacement sensor (LDS) placed right below the cable for the reference cable displacement measurement, (d) accelerometer installed on the cable for reference acceleration measurement, and (e) FOV of the camera and selected ROIs

The proposed technique was first validated via laboratory testing of an 11.8 m long pedestrian bridge cable (Figure 7). The mass per unit length of the cable was 4.229 kg/m, and the diameter was 42.2 mm with a protective shell. A smartphone (iPhone 11) was used as the VIS. An open-source iOS app [29] was used to record 2160×3840 pixel resolution images at 30 Hz and inertial measurements at 100 Hz. iPhone 11 has a built-in 6-axis digital IMU sensor that integrates a 3-axis accelerometer and a 3-axis gyroscope. The FOV of the VIS and the selected ROI for the proposed technique, *i.e.*, ROI 1, are depicted in Figure 7(e). Camera calibration was performed using MATLAB *Camera Calibration Toolbox* to obtain required intrinsic parameters (f and d_{pixel}) of the VIS. The distance between the VIS and the target cable was 1.5 m. The cable was manually excited by pulling and suddenly releasing

the cable in the vertical direction (y -direction). The VIS was placed on a stand connected to a vertical shaker (ELECTRO-SEIS APS-400), and three different excitations were used to generate its motion: (a) Test 1: vertically vibrating the shaker at 1.5 Hz, (b) Test 2: manually tapping the stand along the y -direction, and (c) Test 3: combination of the previous two excitations. A MEMS accelerometer (PCB 3713E112G) with a full-scale range of ± 2 g, a sensitivity of 1000 mV/g, and a noise density of 10 $\mu\text{g}/\sqrt{\text{Hz}}$, was installed on the target cable for measuring reference acceleration. The tension force estimated from the reference acceleration measurement was used as the ground-truth value. The reference displacement at ROI 1 was measured using a KAIS KL3-W400 laser displacement sensor (LDS) with an accuracy of 10 μm .

Two existing cable tension force techniques were used in this study for the performance comparison, as listed in Table 1. The main differences between the proposed method and the two existing techniques are: the method by which the cable displacement is estimated from vision measurements and the way in which the errors produced by the camera motion are compensated for cable displacement estimation. Technique I [17] estimates the cable displacement using a template-matching algorithm and compensates the camera-motion-induced error using a stationary target. Two different stationary targets (ROI S1 and ROI S2 in Figure 7(e)) were separately used for camera motion compensation in this test, and their distances to the camera were 3.8 m and 1.5 m, respectively. Technique II [19] estimates the cable displacement using a boundary-based algorithm and reduces the camera-motion-induced error by calculating the relative displacement between two points within a target cable (ROIs 1 and 2 in Figure 7(e)).

Table 1. Two existing cable tension force estimation techniques used for performance comparison

	Displacement estimation algorithm	Camera motion compensation algorithm	ROIs used
Technique I [17]	Template-matching algorithm	Use camera motion estimated from a stationary target	ROI 1, ROI S1 or ROI S2
Technique II [19]	Boundary-based algorithm	Calculate the relative displacement between two locations of a target cable	ROI 1, ROI 2

3.2 Estimation results

Figure 8 depicts the frequency spectra of the reference acceleration (Figure 8(a)) and displacement (Figure 8(b)) measurements for test 1. The first and second resonance frequencies of the cable appeared at 3.117 Hz and 6.200 Hz, respectively.

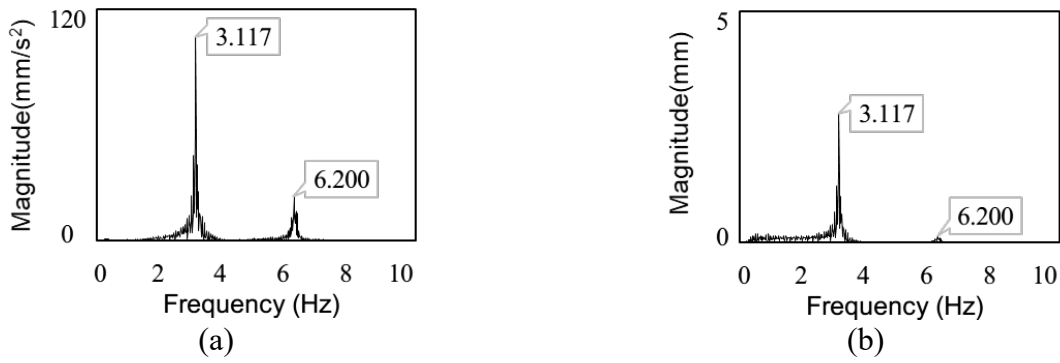


Figure 8. Frequency spectra of (a) reference acceleration measurement and (b) reference displacement measurement obtained from the cable for test 1

Figures 9 and 10 depict the frequency spectra of cable displacements estimated by the three techniques before and after camera motion compensation for test 1, respectively. As depicted in Figure 9, all three techniques identified peaks at 1.500 and 3.100 Hz based on the cable displacement estimated from ROI 1 before camera motion compensation. The second resonance frequency of the cable was not observed because of its small amplitude. In this test, only the camera heave motion was generated, and both the proposed technique and technique I successfully removed the camera-motion-induced peak at 1.500 Hz and estimated the first resonance frequency of the cable at 3.100 Hz after camera motion compensation (Figures 10(a) and 10(b)). Technique 1 used ROI S1 as the stationary target, and the scale factor was estimated using the actual target size in length. No meaningful resonance frequency was observed using technique II because the distance between ROI 1 and ROI 2 was short (approximately 0.5 m) and their relative displacement was negligible, as depicted in Figure 10(c). Because no meaningful resonance frequencies were obtained from technique II for all three tests in this laboratory testing, the corresponding results were not reported hereafter.

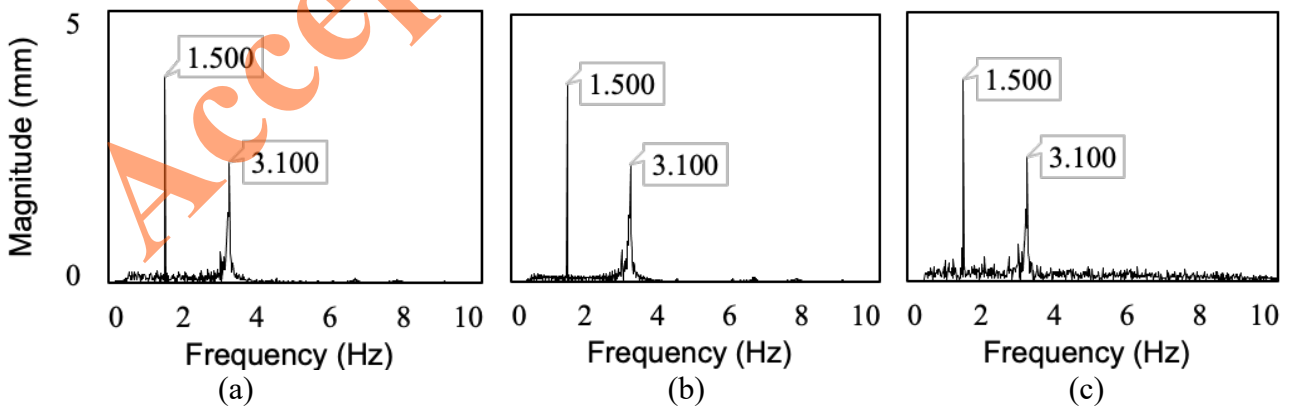


Figure 9. Frequency spectra of cable displacements estimated using ROI 1 for test 1: (a) the proposed technique, (b) technique I, and (c) technique II before camera motion compensation.

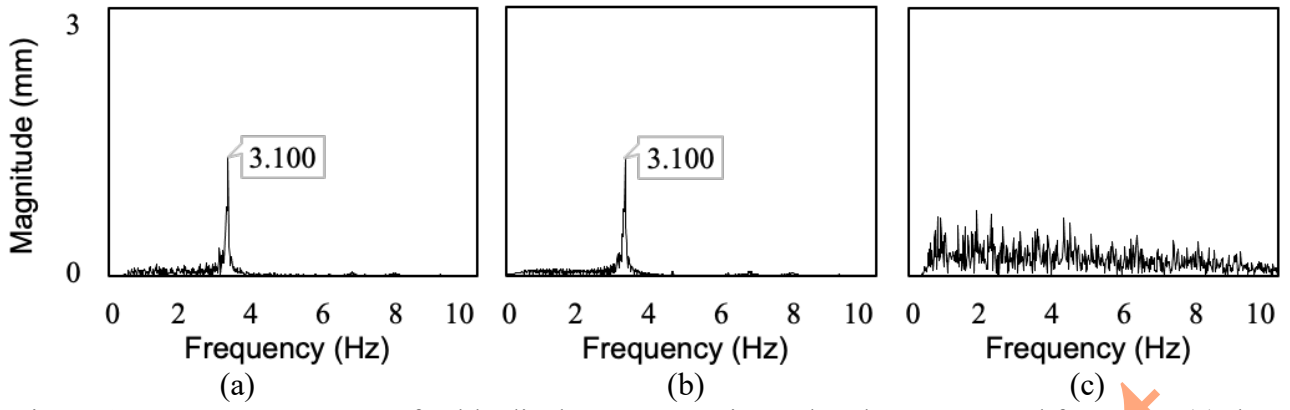


Figure 10. Frequency spectra of cable displacements estimated and compensated for test 1: (a) the proposed technique using ROI 1, (b) technique I using ROI 1 and ROI S1, and (c) technique II using ROI 1 and ROI 2

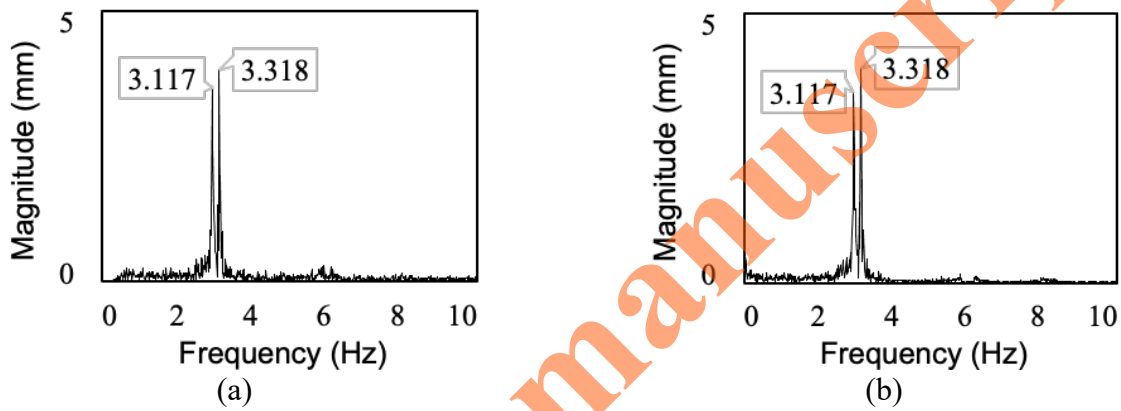


Figure 11. Frequency spectra of cable displacement estimated using ROI 1 for test 2 by (a) the proposed technique and (b) technique I before camera motion compensation

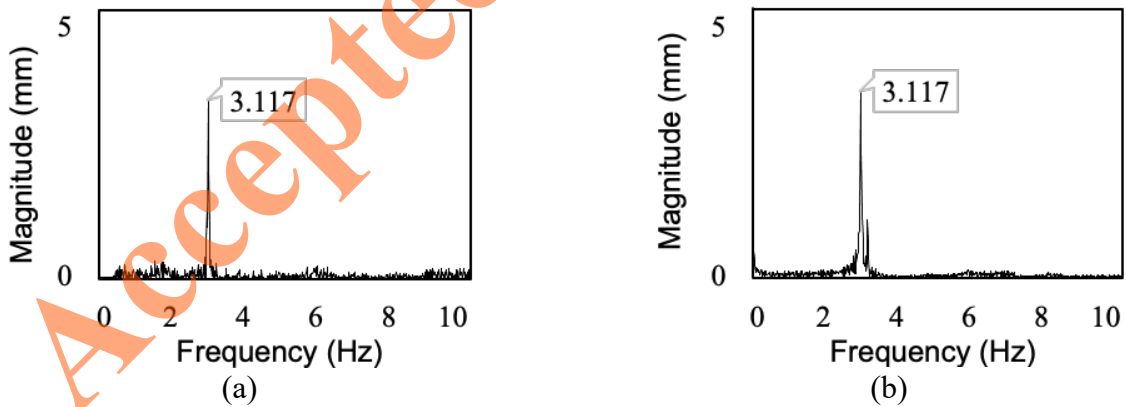


Figure 12. Frequency spectra of the displacements estimated and compensated for test 2 by (a) the proposed technique using ROI 1, and (b) technique I using ROI 1 and ROI S1

Figures 11 and 12 depict the frequency spectra of cable displacements estimated by the proposed technique and technique I before and after camera motion compensation for test 2, respectively. As depicted in Figure 11, both techniques identified peaks at 3.117 and 3.318 Hz based on the cable displacement estimated from ROI 1 before camera motion compensation. In this test, the camera pitch

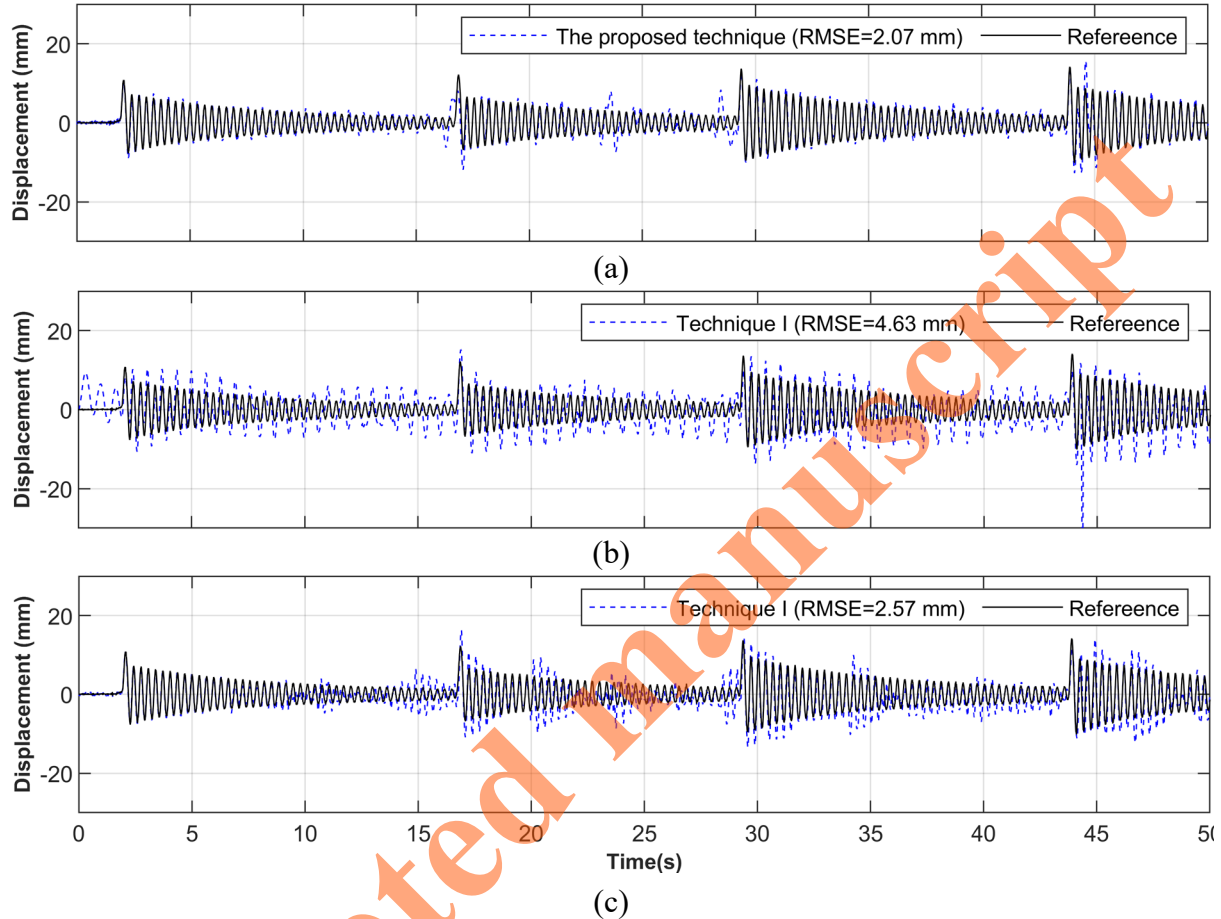


Figure 13. Displacements estimated and compensated by (a) the proposed technique using ROI 1, (b) technique I using ROI 1 and ROI S1, and (c) technique I using ROI 1 and ROI S2

Figure 13 compares the reference displacement from the LDS and the displacements estimated by the proposed technique and technique I after camera motion compensation for test 3. In this test, the camera motion included both pitch and heave. The displacement estimated by the proposed technique was in good agreement with the reference displacement (Figure 13(a)). Although there were a few time points where the huge discrepancy between the estimated and reference displacement values were noticeable, their influence on the frequency spectrum and cable tension force estimation was negligible owing to their transient nature. Because the distance between the camera and ROI S1 (3.8 m) was different from the distance between the camera and ROI 1 (1.5 m), technique I could not properly compensate for camera motion using ROI S1 as the stationary target. Therefore, a relatively large discrepancy was observed between the estimated and reference displacements (Figure 13(b)). The performance of technique I was improved by using ROI S2 (Figure 13(c)) instead of ROI S1, because

the camera has an identical distance to both ROI S2 and the target cable.

The frequency spectra of the displacements estimated and compensated by the proposed technique and technique I are depicted in Figure 14. The proposed technique successfully estimated the first resonance frequency of the cable as depicted in Figure 14(a). Technique I identified the first resonance frequency at 3.1 Hz successfully using either ROI S1 or ROI S2 (Figure 14(b) and (c)), but it also picked up the camera-motion-induced peak at 1.5 Hz when ROI S1 was used due to the difference in the distances from the camera to ROI S1 and ROI 1.

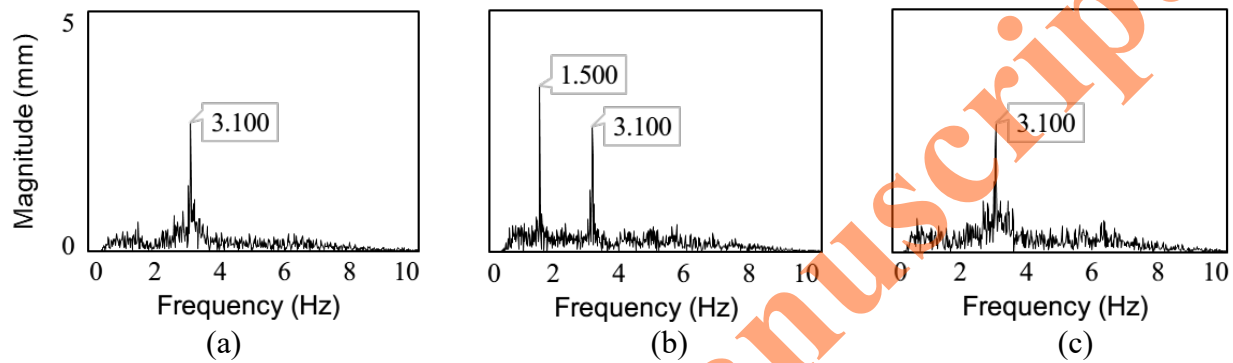


Figure 14. Frequency spectra of the displacements estimated and compensated by (a) the proposed technique using ROI 1, (b) technique I using ROI 1 and ROI S1, and (c) technique I using ROI 1 and ROI S2.

Table 2. Comparison of first resonance frequencies of cable estimated by the proposed technique and technique I

# of tests	Reference (Hz)	Proposed technique		Technique I	
		Estimation (Hz)	Difference (%)	Estimation (Hz)	Difference (%)
Test 1	3.117	3.100	0.55	3.100	0.55
Test 2	3.117	3.117	0	3.117	0
Test 3	3.117	3.100	0.55	1.500 (using ROI S1)	51.88 (using ROI S1)
				3.100 (using ROI S2)	0.55 (using ROI S2)

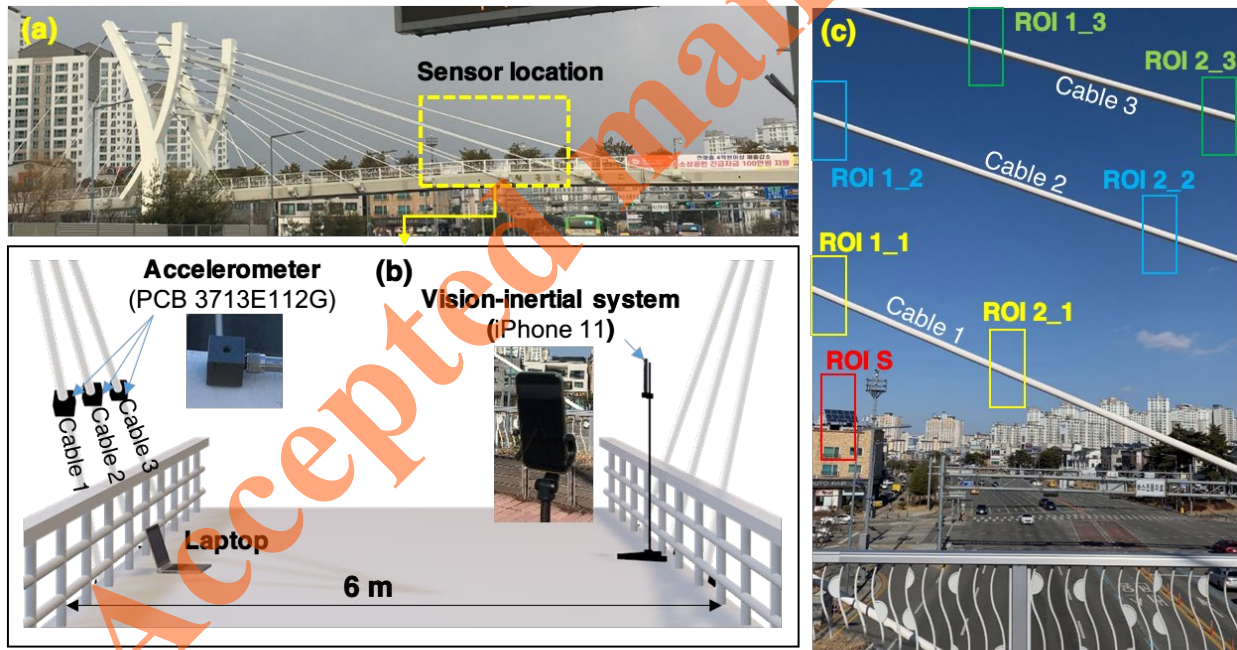
Table 3. Comparison of cable tension forces estimated by the proposed technique and technique I

# of tests	Reference (N)	Proposed technique		Technique I	
		Estimation (N)	Difference (%)	Estimation (N)	Difference (%)
Test 1	22.88	22.63	1.09	22.63	1.09
Test 2	22.88	22.88	0	22.88	0
Test 3	22.88	22.63	1.09	5.30 (using ROI S1)	76.84 (using ROI S1)
				22.63 (using ROI S2)	1.09 (using ROI S2)

The first resonance frequencies and tension forces estimated by both the proposed technique and technique I were compared with the ground-truth values obtained from the reference acceleration measurements listed in Tables 2 and 3. The discrepancies of the proposed technique with respect to the ground truth were less than 0.6% for the first resonance frequency and 1.1% for the tension force. Technique I also properly estimated the first resonance frequency and the tension force with a similar level of accuracy compared to the proposed technique for tests 1 (translation only) and 2 (rotation only). However, technique I can properly estimate the first resonance frequency and the tension force for test 3 (both translation and rotation) only when the camera was placed at an identical distance away from both the additional stationary target (*i.e.*, ROI S2) and the target cable. It should be noted that a stationary target is often located far from the camera under field conditions.

4. Field test on a single-pylon cable-stayed pedestrian bridge

4.1 Experimental setup



ROI 1_1, ROI 2_1: two different points of cable 1; ROI 1_2, ROI 2_2: two different points of cable 2; ROI 1_3, ROI 2_3: two different points of cable 3; ROI S: a stationary target

Figure 15. Overview of single-pylon cable-stayed pedestrian bridge test (a) overview of bridge, (b) experimental setup, and (c) the FOV of the camera and the selected ROIs

The proposed technique was further validated on a single-pylon cable-stayed pedestrian bridge in Daejeon, South Korea (Figure 15(a)). This pedestrian bridge is 65 m long in the main span and 6 m wide. The experimental setup is illustrated in Figure 15(b). The VIS (iPhone 11) identical to the one

used in the previous laboratory experiment was used again as a VIS, and was placed on a stand (Figure 15(b)) to capture three target cables within the FOV of the camera (Figure 15(c)). Three MEMS accelerometers (PCB 3713E112G) were installed on these cables separately (Figure 15(b)) to estimate the ground truth of the cable tension force. Both the cables and the stand were excited by wind and pedestrians crossing the bridge. The wind speed was 6.8 m/s according to meteorological data. As depicted in Figure 15(c), two ROIs were selected for each cable, *i.e.*, ROI 1_1 and ROI 2_1 for cable 1, ROI 1_2 and ROI 2_2 for cable 2, and ROI 1_3 and ROI 2_3 for cable 3, and ROI S was selected as the stationary target. All other test parameters were kept identical to those used in the previous laboratory test.

4.2 Estimation results

Figure 16 depicts the frequency spectra of the reference acceleration measurements obtained from the three cables. Two resonance frequencies at 2.016 and 3.999 Hz for cable 1, two resonance frequencies at 1.650 and 3.233 Hz for cable 2, and four resonance frequencies at 1.160, 1.900, 2.879, and 3.833 Hz for cable 3 were identified.

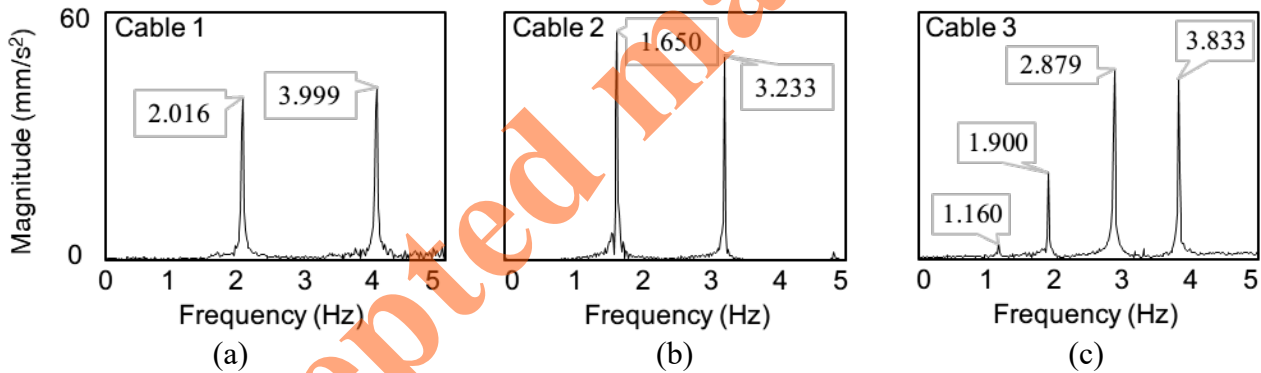


Figure 16. Frequency spectra of the reference acceleration measurements for (a) cable 1, (b) cable 2, and (c) cable 3

The frequency spectra of cable 1 displacement estimated by the three techniques are depicted in Figures 17-19. As illustrated in Figures 17(a), 18(a), and 19(a), all the three techniques identified peaks at 1.850, 1.883, 1.917, 2.017, and 4.000 Hz based on the cable displacement estimated from ROI 1_1 before camera motion compensation. After camera motion compensation, the proposed technique removed the frequency peaks produced by the vibration of the VIS and retained only the peaks truly relevant to the cable vibration (two resonance frequencies at 2.017 and 4.000 Hz). The differences between these frequency values and those obtained from the reference acceleration measurements were less than 0.05%.

Because the distance between the camera and the stationary target (ROI S) (approximately 65 m)

was significantly longer than the distance between the camera and the target cable (ROI 1_1) (6 m), the camera motion estimated from ROI S was very noisy and it was not equal to the camera-motion-induced error in the estimated cable displacement. Thus, technique I removed the camera-motion-induced peaks at 1.883 and 1.917 Hz, but could not eliminate the other camera-motion-induced peak at 1.850 Hz even after camera motion compensation. Consequently, without eliminating all camera-motion-induced peaks, technique I produced an additional artifact resonance frequency at 1.850 Hz (Figure 18(b)). In addition, the actual second resonance frequency of the cable at 4.000 Hz was buried under the increased noise level, as depicted in Figure 18(b).

Figure 19(a) and 19(b) depict the frequency spectra of cable 1 displacements estimated from ROI 1_1 and ROI 2_1 using technique II, respectively. Figure 19(c) shows the frequency spectrum after compensating the camera-motion-induced error by computing the relative displacement between ROI 1_1 and ROI 2_1. After displacement compensation, technique II properly estimated the first resonance frequency of the cable, but the second resonance frequency disappeared. Negligible relative displacement between ROI 1_1 and ROI 2_1, which were approximately 2 m apart from each other, resulted in the oblivion of the second resonance frequency from the frequency spectrum.

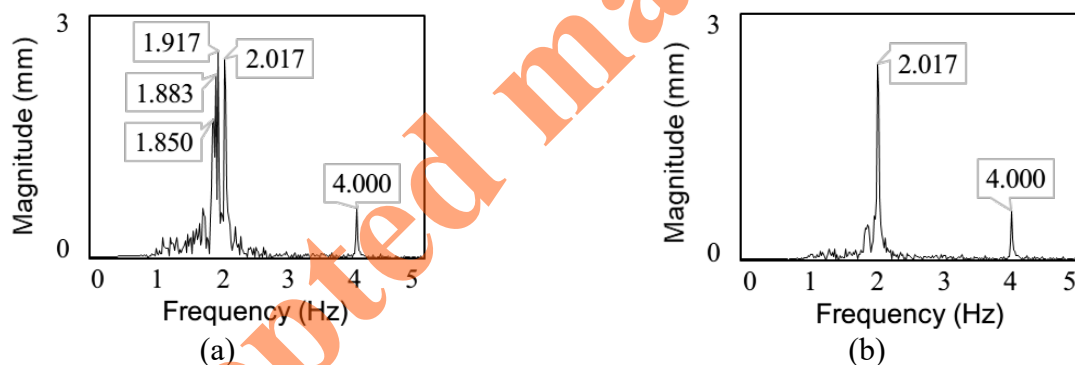


Figure 17. Frequency spectra of cable 1 displacements estimated from ROI 1_1 using the proposed technique (a) before and (b) after camera motion compensation

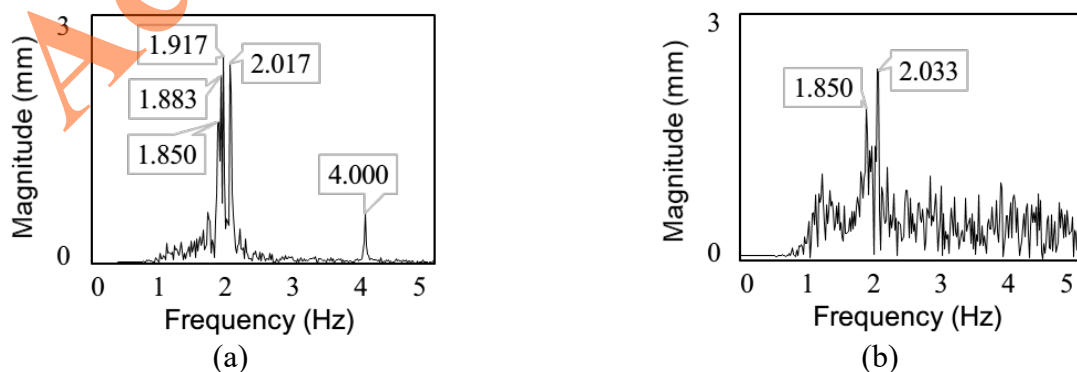


Figure 18. Frequency spectra of cable 1 displacements estimated from ROI 1_1 using technique I (a) before and (b) after camera motion compensation using ROI S

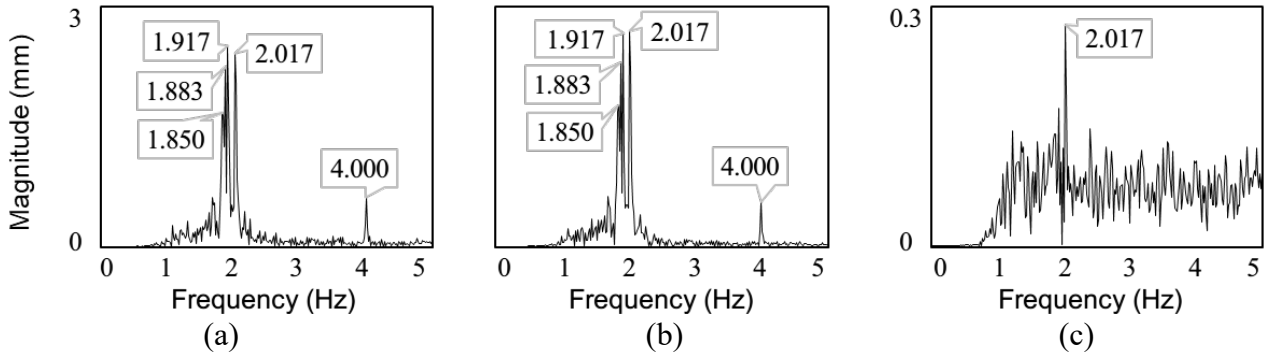


Figure 19. Frequency spectra of cable 1 displacements estimated from (a) ROI 1_1 and (b) ROI 2_1 before camera motion compensation, and (c) after camera motion compensation using technique II

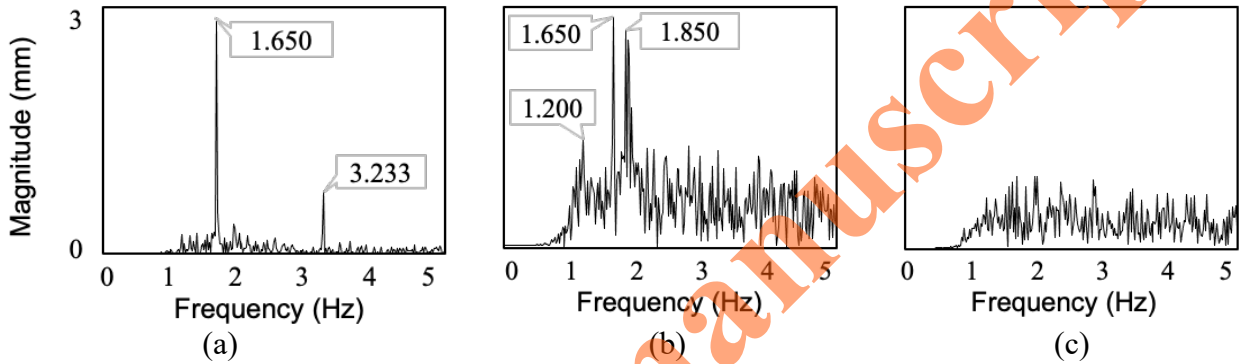


Figure 20. Frequency spectra of cable 2 displacements estimated and compensated by (a) the proposed technique using ROI 1_2, (b) technique I using ROI 1_2 and ROI 2_2, and (c) technique II using ROI 1_2 and ROI S

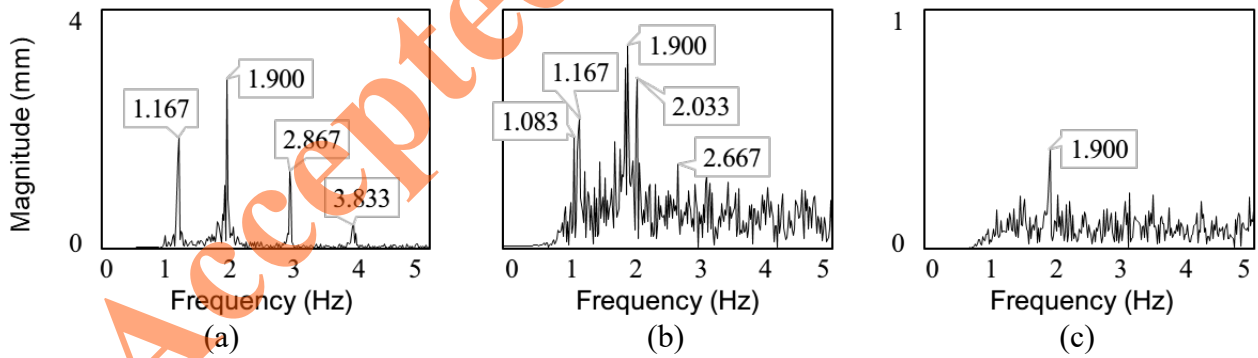


Figure 21. Frequency spectra of cable 3 displacements estimated and compensated by (a) the proposed technique using ROI 1_3, (b) technique I using ROI 1_3 and ROI 2_3, and (c) technique II using ROI 1_3 and ROI S

The frequency spectra of cables 2 and 3 displacements estimated by the three techniques after camera motion compensation are shown in Figures 20 and 21, respectively. The proposed technique correctly estimated two resonance frequencies of cable 2 (Figure 20(a)) and four resonance frequencies of cable 3 (Figure 21(a)). However, technique I could not fully eliminate camera-motion-induced peaks, further resulting in inaccurate resonance frequency estimation for both cables 2 and 3. (Figures 20(b)

and 21(b)). Using technique II, no meaningful resonance frequency was observed for cable 2 (Figure 20(c)). Furthermore, the frequency peak at 1.900 Hz was mistaken as the first resonance frequency of cable 3 because the actual first resonance frequencies was suppressed from the frequency spectrum (Figure 21(c)).

The first resonance frequency estimated by the three techniques were compared with the ground-truth values obtained from the reference acceleration measurements listed in Table 4. The proposed technique estimated the first resonance frequencies properly for all the three cables with a discrepancy of less than 1%. Because technique I could not fully eliminate the camera-motion-induced error, the discrepancy between estimated resonance frequencies and reference values was as high as 27%. Technique II estimated the first resonance frequency of cable 1 correctly but could not successfully estimate the first resonance frequencies of cables 2 and 3.

Finally, the differences between the cable tension forces estimated by the three techniques and the reference acceleration measurements are summarized in Table 5. The proposed technique estimated the tension forces for all the three cables with a difference of less than 1.3%. Technique I estimated the cable tension force with a large discrepancy of up to 47%, and technique II was able to estimate the tension force of cable 1 only.

Table 4. Comparison of first resonance frequencies estimated by the three techniques (from in-situ single-pylon cable-stayed pedestrian bridge test)

Cables #	Reference (Hz)	Proposed		Technique I		Technique II	
		Estimation (Hz)	Difference (%)	Estimation (Hz)	Difference (%)	Estimation (Hz)	Difference (%)
1	2.016	2.017	0.05	1.850	8.23	2.017	0.05
2	1.650	1.650	0	1.200	27.27	N/A	N/A
3	1.160	1.167	0.60	1.083	6.64	1.900	63.79

Table 5. Differences between the cable tension forces estimated by the three techniques and the reference acceleration measurement (from in-situ single-pylon cable-stayed pedestrian bridge test)

# of cables	Proposed (%)	Technique I (%)	Technique II (%)
1	0.10	15.79	0.10
2	0.31	47.11	N/A
3	1.21	12.84	168.28

5. Conclusion

In this study, a noncontact cable tension force estimation technique was developed using a VIS installed on a vibrating reference point. Initially, the cable displacement was estimated by applying the proposed contour-based algorithm to the vision images obtained from the VIS. Thereafter, the vibration

of the VIS itself was estimated using the inertial measurements of the VIS and compensated for the improved displacement estimation. Finally, the cable tension force was estimated from the compensated cable displacement using taut string theory. The feasibility of the proposed technique for cable tension force estimation was validated through a laboratory test on a full-scale pedestrian bridge cable and a field test on a single-pylon cable-stayed pedestrian bridge. The proposed technique was able to properly estimate cable tension forces with less than 1.3% differences compared to those estimated from the reference accelerometer measurements in both laboratory and field tests. However, there are several limitations. First, the background of a cable is assumed to be textureless, but the assumption may be no longer valid under bad weather conditions. Future work is warranted to address this issue. Second, this study used a smartphone as a VIS, but the misalignment between the IMU and camera of the smartphone and the optical image stabilization (OIS) system included in the camera may cause additional errors in the camera motion compensation. To fully avoid this issue, a VIS should be developed by installing an IMU sensor at the center of gravity of a vision camera (without any OIS system). Last, the distance between the VIS and the target cable was limited to 6 m in this study, which may not be sufficient for large-scale bridges. A follow-up study is warranted to advance the sensing range of the proposed technique.

Acknowledgment

This work was supported by the National Research Foundation of Korea (NRF) grant funded by the Korean government (MSIT) (No. 2017R1A5A1014883).

References

- [1] D.-H. Yang, T.-H. Yi, H.-N. Li, Y.-F. Zhang, Correlation-Based Estimation Method for Cable-Stayed Bridge Girder Deflection Variability under Thermal Action, *Journal of Performance of Constructed Facilities*. 32 (2018) 04018070. [https://doi.org/10.1061/\(ASCE\)CF.1943-5509.0001212](https://doi.org/10.1061/(ASCE)CF.1943-5509.0001212).
- [2] D.-H. Yang, T.-H. Yi, H.-N. Li, H. Liu, T. Liu, Train-induced dynamic behavior analysis of longitudinal girder in cable-stayed bridge, *Smart structures and systems*. 21 (2018) 549–559. <https://doi.org/10.12989/sss.2018.21.5.549>.
- [3] A. Camara, M.A. Astiz, A.J. Ye, Fundamental mode estimation for modern cable-stayed bridges considering the tower flexibility, *Journal of Bridge Engineering*. 19 (2014) 04014015. [https://doi.org/10.1061/\(ASCE\)BE.1943-5592.0000585](https://doi.org/10.1061/(ASCE)BE.1943-5592.0000585).
- [4] S. Cho, J. Yim, S.W. Shin, H.-J. Jung, C.-B. Yun, M.L. Wang, Comparative Field Study of Cable Tension Measurement for a Cable-Stayed Bridge, *Journal of Bridge Engineering*. 18 (2013) 748–757. [https://doi.org/10.1061/\(ASCE\)BE.1943-5592.0000421](https://doi.org/10.1061/(ASCE)BE.1943-5592.0000421).
- [5] N. Kaur, S. Goyal, K. Anand, G.K. Sahu, A cost-effective approach for assessment of pre-stressing

-
- 388 force in bridges using piezoelectric transducers, *Measurement*. 168 (2021) 108324.
389 <https://doi.org/10.1016/j.measurement.2020.108324>.
- 390 [6] Y.-S. Kim, H.-J. Sung, H.-W. Kim, J.-M. Kim, Monitoring of tension force and load transfer of
391 ground anchor by using optical FBG sensors embedded tendon, *Smart Structures and Systems*. 7 (2011)
392 303–317. <https://doi.org/10.12989/sss.2011.7.4.303>.
- 393 [7] E. Nazarian, F. Ansari, X. Zhang, T. Taylor, Detection of Tension Loss in Cables of Cable-Stayed
394 Bridges by Distributed Monitoring of Bridge Deck Strains, *Journal of Structural Engineering*. 142
395 (2016) 04016018. [https://doi.org/10.1061/\(ASCE\)ST.1943-541X.0001463](https://doi.org/10.1061/(ASCE)ST.1943-541X.0001463).
- 396 [8] Z. Fang, J. Wang, Practical Formula for Cable Tension Estimation by Vibration Method, *Journal*
397 *of Bridge Engineering*. 17 (2012) 161–164. [https://doi.org/10.1061/\(ASCE\)BE.1943-5592.0000200](https://doi.org/10.1061/(ASCE)BE.1943-5592.0000200).
- 398 [9] B.H. Kim, T. Park, Estimation of cable tension force using the frequency-based system
399 identification method, *J. Sound Vib*. 304 (2007) 660–676. <https://doi.org/10.1016/j.jsv.2007.03.012>.
- 400 [10] G. Feltrin, J. Meyer, R. Bischoff, O. Saukh, A wireless sensor network for force monitoring of
401 cable stays, in: *Proceedings of the 3rd International Conference on Bridge Maintenance, Safety and*
402 *Management, IABMAS, 2006*.
- 403 [11] R. Geier, G. De Roeck, R. Flesch, Accurate cable force determination using ambient vibration
404 measurements, *Structure and Infrastructure Engineering*. 2 (2006) 43–52.
405 <https://doi.org/10.1080/15732470500253123>.
- 406 [12] S. Xue, R. Shen, Real time cable force identification by short time sparse time domain algorithm
407 with half wave, *Measurement*. 152 (2020) 107355.
408 <https://doi.org/10.1016/j.measurement.2019.107355>.
- 409 [13] J. Yim, M.L. Wang, S.W. Shin, C.-B. Yun, H.-J. Jung, J.-T. Kim, S.-H. Eem, Field application of
410 elasto-magnetic stress sensors for monitoring of cable tension force in cable-stayed bridges, *Smart*
411 *Structures and Systems*. 12 (2013) 465–482. https://doi.org/10.12989/sss.2013.12.3_4.465.
- 412 [14] C. Cappello, D. Zonta, H. Ait Laasri, B. Glisic, M. Wang, Calibration of Elasto-Magnetic Sensors
413 on In-Service Cable-Stayed Bridges for Stress Monitoring, *Sensors*. 18 (2018) 466.
414 <https://doi.org/10.3390/s18020466>.
- 415 [15] J.-M. Kim, J. Lee, H. Sohn, Automatic measurement and warning of tension force reduction in a
416 PT tendon using eddy current sensing, *NDT & E International*. 87 (2017) 93–99.
417 <https://doi.org/10.1016/j.ndteint.2017.02.002>.
- 418 [16] S.-W. Kim, B.-G. Jeon, N.-S. Kim, J.-C. Park, Vision-based monitoring system for evaluating
419 cable tensile forces on a cable-stayed bridge, *STRUCTURAL HEALTH MONITORING-AN*

- INTERNATIONAL JOURNAL. 12 (2013) 440–456. <https://doi.org/10.1177/1475921713500513>.
- [17] S.-W. Kim, N.-S. Kim, Dynamic characteristics of suspension bridge hanger cables using digital image processing, *NDT & E International*. 59 (2013) 25–33. <https://doi.org/10.1016/j.ndteint.2013.05.002>.
- [18] D. Feng, T. Scarangelo, M.Q. Feng, Q. Ye, Cable tension force estimate using novel noncontact vision-based sensor, *Measurement*. 99 (2017) 44–52. <https://doi.org/10.1016/j.measurement.2016.12.020>.
- [19] Y. Tian, C. Zhang, S. Jiang, J. Zhang, W. Duan, Noncontact cable force estimation with unmanned aerial vehicle and computer vision, *Computer-Aided Civil and Infrastructure Engineering*. (2020). <https://doi.org/10.1111/mice.12567>.
- [20] Y. Xu, J. Brownjohn, D. Kong, A non-contact vision-based system for multipoint displacement monitoring in a cable-stayed footbridge, *Structural Control & Health Monitoring*. 25 (2018). <https://doi.org/10.1002/stc.2155>.
- [21] T. Khuc, F.N. Catbas, Computer vision-based displacement and vibration monitoring without using physical target on structures, *Structure and Infrastructure Engineering*. 13 (2017) 505–516. <https://doi.org/10.1080/15732479.2016.1164729>.
- [22] D. Lydon, M. Lydon, S. Taylor, J.M. Del Rincon, D. Hester, J. Brownjohn, Development and field testing of a vision-based displacement system using a low cost wireless action camera, *Mechanical Systems and Signal Processing*. 121 (2019) 343–358. <https://doi.org/10.1016/j.ymssp.2018.11.015>.
- [23] H. Yoon, J. Shin, B.F. Spencer Jr, Structural displacement measurement using an unmanned aerial system, *Computer-Aided Civil and Infrastructure Engineering*. 33 (2018) 183–192. <https://doi.org/10.1111/mice.12338>.
- [24] Z. Ma, J. Choi, H. Sohn, Real-time structural displacement estimation by fusing asynchronous acceleration and computer vision measurements, *Comput.-Aided Civ. Infrastruct. Eng.* (2021). <https://doi.org/10.1111/mice.12767>.
- [25] Z. Ma, J. Choi, P. Liu, H. Sohn, Structural displacement estimation by fusing vision camera and accelerometer using hybrid computer vision algorithm and adaptive multi-rate Kalman filter, *Automation in Construction*. 140 (2022) 104338. <https://doi.org/10.1016/j.autcon.2022.104338>.
- [26] J. Lee, K.-C. Lee, S. Jeong, Y.-J. Lee, S.-H. Sim, Long-term displacement measurement of full-scale bridges using camera ego-motion compensation, *Mechanical Systems and Signal Processing*. 140 (2020). <https://doi.org/10.1016/j.ymssp.2020.106651>.
- [27] R. Grompone von Gioi, J. Jakubowicz, J.-M. Morel, G. Randall, LSD: A Fast Line Segment

-
- 452 Detector with a False Detection Control, IEEE Transactions on Pattern Analysis and Machine
453 Intelligence. 32 (2010) 722–732. <https://doi.org/10.1109/TPAMI.2008.300>.
- 454 [28]Y. Yang, L. Sanchez, H. Zhang, A. Roeder, J. Bowlan, J. Crochet, C. Farrar, D. Mascareñas,
455 Estimation of full-field, full-order experimental modal model of cable vibration from digital video
456 measurements with physics-guided unsupervised machine learning and computer vision, Structural
457 Control and Health Monitoring. 26 (2019) e2358. <https://doi.org/10.1002/stc.2358>.
- 458 [29]J. Huai, Y. Zhang, A. Yilmaz, The Mobile AR Sensor Logger for Android and iOS devices, in:
459 2019 IEEE SENSORS, 2019: pp. 1–4. <https://doi.org/10.1109/SENSORS43011.2019.8956816>.

460

Accepted manuscript